PROCEEDINGS A

royalsocietypublishing.org/journal/rspa

Research

Cite this article: Li W, Lipton R, Maier M. 2021 Lorentz resonance in the homogenization of plasmonic crystals. *Proc. R. Soc. A* **477**: 20210609.
https://doi.org/10.1098/rspa.2021.0609

Received: 27 July 2021
Accepted: 26 October 2021

Subject Areas:
applied mathematics, electromagnetism, differential equations

Keywords:
homogenization, Maxwell's equations, plasmonic crystals, Lorentz resonance

Author for correspondence:
W. Li
e-mail: wei.li@depaul.edu

Lorentz resonance in the homogenization of plasmonic crystals

W. Li[1], R. Lipton[2] and M. Maier[3]

[1]Department of Mathematical Sciences, DePaul University, Chicago, IL 60614, USA
[2]Department of Mathematics, Louisiana State University, Baton Rouge, LA 70803, USA
[3]Department of Mathematics, Texas A&M University, College Station, TX 77843, USA

WL, 0000-0003-4098-4705; RL, 0000-0002-1382-3204; MM, 0000-0002-4960-5217

We explain the Lorentz resonances in plasmonic crystals that consist of two-dimensional nano-dielectric inclusions as the interaction between resonant material properties and geometric resonances of electrostatic nature. One example of such plasmonic crystals are graphene nanosheets that are periodically arranged within a non-magnetic bulk dielectric. We identify local geometric resonances on the length scale of the small-scale period. From a materials perspective, the graphene surface exhibits a dispersive surface conductance captured by the Drude model. Together these phenomena conspire to generate Lorentz resonances at frequencies controlled by the surface geometry and the surface conductance. The Lorentz resonances found in the frequency response of the effective dielectric tensor of the bulk metamaterial are shown to be given by an explicit formula, in which material properties and geometric resonances are decoupled. This formula is rigorous and obtained directly from corrector fields describing local electrostatic fields inside the heterogeneous structure. Our analytical findings can serve as an efficient computational tool to describe the general frequency dependence of periodic optical devices. As a concrete example, we investigate two prototypical geometries composed of nanotubes and nanoribbons.

THE ROYAL SOCIETY PUBLISHING

1. Introduction

Novel frequency-dependent electromagnetic behaviour can be generated by patterned dispersive dielectric metamaterials undergoing localized geometric resonance. Here the period of the pattern lies below the wavelength of operation. Examples include plasmonic metasurfaces [1,2], band gaps generated by periodic configurations of local plasmon resonators [3] and beam steering [4]. In this work we contribute to the *analytic* understanding of such periodic optical devices by investigating the role of local (frequency-independent) geometric features and (frequency-dependent) material properties. In particular, we explain the appearance of Lorentz resonances generated by periodically patterned dispersive dielectrics *as the interaction* between resonant material properties and local geometric resonances of electrostatic nature.

Concretely, we shall examine the optical frequency response of plasmonic crystals formed by two-dimensional material inclusions (such as graphene) embedded in a non-magnetic bulk dielectric host. We use a Drude model for the local conductivity response of the two-dimensional material but allow for a fairly general periodic geometry, including, for example, graphene nanoribbons or graphene nanotubes. In such geometries, frequency-independent geometric resonances will be identified and characterized that occur on the length scale of the period of the two-dimensional material inclusions. These local resonances are novel as they exist both on the surface of the sheets and in the bulk. Together with the dispersive surface conductance of the two-dimensional material, both phenomena conspire to generate Lorentz resonances in the effective optical frequency response of the metamaterial. The resonance frequencies are controlled by the surface geometry and the surface conductance.

The Lorentz resonances for the effective dielectric tensor or equivalently the effective index of refraction for the bulk metamaterial are shown to be given by an explicit formula. This formula is rigorous and obtained directly from the corrector fields describing local electrostatic fields inside the heterogeneous structure. The local boundary value problem for the correctors follows from the periodic homogenization theory for Maxwell's equations developed in [5–9]. The formula for the effective dielectric constant obtained here is notable in that the local geometric resonances and local surface conductivity are uncoupled. This offers the opportunity for efficient computation of the effective dielectric constant through the computation of the local geometric resonances that are independent of the specific material properties. The interaction between geometry and material dispersion is displayed explicitly in the rigorously derived formula.

In detail, our contributions with the current work can be summarized as follows.

— We describe the interplay between frequency-independent geometric nanoscale resonances and frequency-dependent local conductivity models that results in Lorentz resonances in the effective optical frequency response. We derive an explicit formula for the frequency response rigorously from a mathematical homogenization theory for Maxwell's equations for periodic two-dimensional material inclusions.
— The spectral decomposition is enabled by identifying an underlying compact self-adjoint operator on a proper function space. This was done by symmetrizing a non-Hermitian operator.
— We discuss how to use the analytic result for computing approximations on the frequency response of periodic optical configurations. This approach offers a significant saving in computational resources because only one frequency-independent geometric eigenvalue problem has to be computed, in contrast to computing the corrector field for a huge number of fixed frequencies [6,10].
— We examine two prototypical geometries—a nanotube and a nanoribbon configuration—in more detail. The latter is analytically and computationally much more challenging owing to singularities at the interior two-dimensional material edges. We discuss decay estimates and examine the approximation quality of our computational approach.

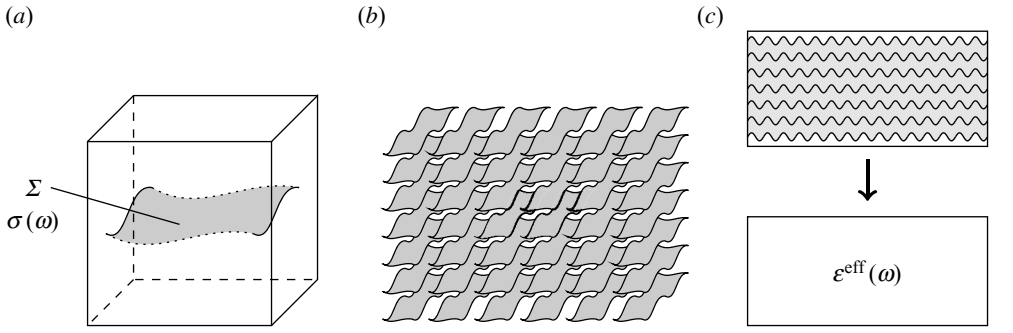

Figure 1. The homogenization procedure: (*a*) the nanoscale unit cell Y consisting of two-dimensional metallic inclusions Σ with surface conductivity $\sigma(\omega)$ in an ambient host material with permittivity ε; (*b*) the plasmonic crystal formed by many scaled and repeated copies of Y in every space dimension; (*c*) a schematic of the homogenization process in which the nanoscale structure is replace by a homogeneous material with effective permittivity ε^{eff}.

(a) Background: homogenization of plasmonic crystals

The following analytical investigation is based on a rigorous periodic homogenization theory [5–9]. For the sake of simplicity, we will base our analytical investigation on a slightly simplified setting that we quickly outline here.

Consider a three-dimensional plasmonic crystal consisting of periodic copies of a *representative volume element* Y, which incorporates nanoscale inclusions given by two-dimensional material surfaces (figure 1) of reasonably arbitrary shape (specified in §1b and appendix B). The conductivity of the surfaces is assumed to obey the Drude model,

$$\sigma(\omega) = \frac{\mathrm{i}\,\omega_p}{\omega + \mathrm{i}/\tau},$$

where i denotes the imaginary unit, ω is the angular frequency, $\omega_p = 4\alpha \approx 4/137$ is a (rescaled) Drude weight and τ is a material-dependent relaxation time. Here, we have non-dimensionalized all quantities by applying a convenient rescaling [11]: $\tilde{\omega} = \hbar\omega/E_{\mathrm{F}}$, where E_{F} denotes the Fermi energy associated with the two-dimensional material and $\hbar$ is the reduced Planck constant; $\tilde{\sigma}(\tilde{\omega}) = \sqrt{\mu_0/\varepsilon_0}\,\sigma(\omega)$, where μ_0 and ε_0 denote the vacuum permeability and permittivity, respectively. We set the length, height and width of the representative volume element to 1, $Y = [0,1]^3$. Furthermore, we assume that the dielectric host has a uniform and isotropic relative permittivity ε.

It can then be shown [6,11] that for a sufficiently small representative volume element Y and sufficiently many repetitions of Y, i.e. a sufficiently large plasmonic crystal, the *effective* conductivity of the plasmonic crystal is given by a uniform, frequency-dependent conductivity tensor

$$\varepsilon_{ij}^{\text{eff}}(\omega) = \varepsilon\,\delta_{ij} - \frac{\sigma(\omega)}{\mathrm{i}\omega}\int_{\Sigma}\left\{P_T(\boldsymbol{e}_j) + \nabla_T\chi_j(\omega,\boldsymbol{x})\right\}\cdot P_T(\boldsymbol{e}_i)\,\mathrm{d}o_x, \quad i,j = 1,2,3. \tag{1.1}$$

Here, $\boldsymbol{x}$ represents the spatial coordinates, δ_{ij} is Kronecker's Delta, $\boldsymbol{e}_j$ is the jth unit vector, Σ denotes the two-dimensional material surface (embedded in Y), P_T is the projection of a vector onto the two-dimensional tangential space of Σ and $\nabla_T = P_T\nabla$ denotes the tangential gradient (with respect to Σ).

The Y-periodic corrector field $\boldsymbol{\chi}(\boldsymbol{x})$ for closed Σ is the solution of the *cell problem* [6],

$$\begin{cases} \Delta\chi_j(\boldsymbol{x}) = 0 & \text{in } Y\backslash\Sigma, \\ [\chi_j(\boldsymbol{x})]_\Sigma = 0 & \text{on } \Sigma, \\ \varepsilon[\boldsymbol{\nu}\cdot\nabla\chi_j(\boldsymbol{x})]_\Sigma = \frac{\sigma}{\mathrm{i}\omega}\nabla_T\cdot\left(P_T\boldsymbol{e}_j + \nabla_T\chi_j(\boldsymbol{x})\right) & \text{on } \Sigma, \end{cases} \tag{1.2}$$

where $\boldsymbol{\nu}$ is the unit outward normal of Σ at $\boldsymbol{x}$ and $[f](\boldsymbol{x})$ denotes the jump of a quantity f across the surface Σ along the normal direction of Σ, namely

$$[f](\boldsymbol{x}) := \lim_{\alpha \searrow 0} (f(\boldsymbol{x} + \alpha \boldsymbol{\nu}) - f(\boldsymbol{x} - \alpha \boldsymbol{\nu})) \quad \text{for } \boldsymbol{x} \in \Sigma.$$

The novelty of plasmonic materials is that they are used to control light at wavelengths much larger than the characteristic length scale of the period. Thus understanding wave dispersion for such systems through frequency-dependent effective behaviour is quite natural. Recently frequency-dependent effective dispersive behaviour of a finite number of metallic sheets embedded in a dielectric host was compared with direct numerical simulation and shown to agree up to a negligible error [11]. In another work, the frequency dependence of effective properties was mathematically proven to deliver the leading-order dispersive behaviour for subwavelength plasmonic composites; this is rigorously done in theorem 4 of [12]. Last it is noted that the Lorentz resonance for a single particle is not sufficient for understanding periodic subwavelength patterned arrays of inhomogeneities as it ignores close range inter-particle interactions that are captured by the local fields that determine the effective dielectric constant.

(b) Summary of the main result

The objective of our discussion is to decouple the frequency dependence introduced in (1.1) by the surface conductivity and other material parameters from the geometric resonances of the nanostructure. To this end, we introduce an auxiliary spectral problem to identify all $\{\lambda_n\} \subset \mathbb{C}$ for which there exists a φ_n satisfying

$$\begin{cases} \Delta \varphi_n(\boldsymbol{x}) = 0 & \text{in } Y \setminus \Sigma, \\ [\varphi_n(\boldsymbol{x})]_\Sigma = 0 & \text{on } \Sigma, \\ \lambda_n [\boldsymbol{\nu} \cdot \nabla \varphi_n(\boldsymbol{x})]_\Sigma = \nabla_T \cdot \nabla_T \varphi_n(\boldsymbol{x}) & \text{on } \Sigma. \end{cases}$$

Introducing $\eta(\omega) = \sigma(\omega)/\mathrm{i}\omega$ we then show that the effective refractive index in (1.1) can be expressed by the formula

$$\varepsilon_{ij}^{\text{eff}}(\omega) = \varepsilon \delta_{ij} - \eta(\omega) \int_\Sigma P_T(\boldsymbol{e}_j) \cdot P_T(\boldsymbol{e}_i) \, \mathrm{d}o_x - \sum_{n=1}^{\infty} \frac{\lambda_n \, \eta^2(\omega)}{\varepsilon - \lambda_n \, \eta(\omega)} \, M_{jn} \, \overline{M_{in}}, \tag{1.3}$$

where the factors M_{jn} are defined as

$$M_{jn} = \int_\Sigma P_T(\boldsymbol{e}_j) \cdot \nabla_T \overline{\varphi}_n(\boldsymbol{x}) \, \mathrm{d}o_x, \quad j = 1, 2, 3, \; n = 1, 2, \ldots.$$

The important property of this formula is that the integrals only depend on geometry, and the coefficients only depend on frequency. Equating the real part of the denominator in the coefficients of (1.3) to zero recovers an explicit resonance frequency $\omega_{R,n}$ for which the contribution of the nth term of the sum may become dominant,

$$\omega_{R,n} = \sqrt{\omega_{0,n}^2 - \frac{1}{(2\tau)^2}}, \quad \text{where } \omega_{0,n}^2 = \frac{\lambda_n \omega_p}{\varepsilon}, \quad n = 1, 2, \ldots.$$

(c) Past works

Plasmonic crystals based on patterned dispersive dielectric two-dimensional material inclusions have made possible an unprecedented wealth of novel functional optical devices [13–18]. Possible applications range from optical holography [19], tunable metamaterials [20] and cloaking [21] to subwavelength focusing lenses [22].

The analytical approach taken here is motivated by earlier observations of local resonances occurring at the length scale of the microgeometry. Electrostatic resonances identified at the length scale of composite geometry were shown to control the effective dielectric response associated with crystals made from non-dispersive dielectric inclusions in the pioneering work of [23,24].

The associated representation formulae based on local resonances were extended and applied to bound the effective dielectric response [25–27]. Most recently local electrostatic and plasmonic resonances have been used to construct non-magnetic double negative metamaterials in the near infrared [12] and design photonic band gap materials [28].

The current work advances the understanding of effective dielectric behaviour by discovering and subsequently taking advantage of local resonances supported both on surfaces and in the bulk for generating Lorentz resonances at frequencies explicitly controlled by the microstructure.

(d) Paper organization

The remainder of the paper is organized as follows. In §2, we introduce the analytical setting and discuss our spectral decomposition result. The emerging Lorentz resonance and an application to inverse optical design are discussed in §3. A computational framework based on the spectral decomposition is outlined in §4 and two prototypical geometries are computationally analysed. We discuss implications and conclude in §5.

Analytical technicalities concerning the spectral decomposition result on closed and open surfaces are outlined in appendices A and B. We summarize some explicit analytical formulae for the solution of the geometric eigenvalue problem in appendix C.

2. Spectral decomposition

In this section, we introduce and characterize an auxiliary spectral problem that enables us to derive the spectral decomposition (1.3) of the cell problem (1.2). For the sake of argument, we keep the discussion in this section on a formal level. A mathematically rigorous formulation of the spectral decomposition for general classes of *closed* and *open* two-dimensional dielectric inclusions Σ is given in appendices A and B, respectively. Here, a closed inclusion Σ is a Y-periodic two-dimensional surface that does not have any one-dimensional edges in the interior of Y. Similarly, an open inclusion Σ is a Y-periodic two-dimensional surface that exhibits an edge in the interior of Y (figure 1).

(a) An auxiliary eigenvalue problem

As a first step, we introduce an auxiliary eigenvalue problem that is closely related to the cell problem (1.2) of the homogenization process. By removing the forcing $P_T e_j$ and replacing the quotient $i\omega\varepsilon/\sigma$ by a real-valued eigenvalue λ one arrives at the spectral problem: find all pairs of eigenvalues $\lambda \in \mathbb{R}$ and corresponding square-integrable eigenfunctions φ such that

$$\begin{cases} \Delta\varphi(\boldsymbol{x}) = 0 & \text{in } Y\setminus\Sigma, \\ [\phi(\boldsymbol{x})]_\Sigma = 0 & \text{on } \Sigma, \\ \lambda[\boldsymbol{\nu}\cdot\nabla\varphi(\boldsymbol{x})]_\Sigma = \Delta_T\varphi(\boldsymbol{x}) & \text{on } \Sigma. \end{cases} \tag{2.1}$$

Here, $\boldsymbol{\nu}$ is again the unit outward normal of Σ at $\boldsymbol{x}$. We have set $\Delta_T := \nabla_T\cdot\nabla_T$ and $[f](\boldsymbol{x})$ denotes the jump of a quantity f across the surface Σ along the normal direction of Σ, namely

$$[f](\boldsymbol{x}) := \lim_{\alpha\searrow 0}(f(\boldsymbol{x}+\alpha\boldsymbol{\nu}) - f(\boldsymbol{x}-\alpha\boldsymbol{\nu})) \quad \text{for } \boldsymbol{x}\in\Sigma.$$

Eigenvalue problem (2.1) is certainly well posed and will admit an orthonormal basis of square-integrable eigenfunctions provided one can identify an underlying self-adjoint and compact linear operator. For all square-integrable *densities* $\gamma(\boldsymbol{x})$ defined on the surface Σ we thus introduce the periodic single-layer operator $\mathbf{S}\gamma$ by setting

$$(\mathbf{S}\gamma)(\boldsymbol{x}) := \int_\Sigma G_{\text{per}}(\boldsymbol{x}-\boldsymbol{y})\gamma(\boldsymbol{y})\,\mathrm{d}o_y \quad \text{and} \quad \boldsymbol{x}\in Y. \tag{2.2}$$

Here, G_{per} is the periodic Green's function of the periodic Laplace problem, namely

$$G_{\mathrm{per}}(\boldsymbol{x}) := \sum_{\vec{z}\in\mathbb{Z}^n} G_0(\vec{z}+\boldsymbol{x}) \quad \text{and} \quad G_0(x) := -\frac{1}{4\pi|x|}.$$

The single-layer operator $\mathbf{S}$ is constructed in such a way that $\mathbf{S}\gamma$ satisfies

$$\Delta \mathbf{S}\gamma = 0 \quad \text{in } \Omega\backslash\Sigma, \quad [\mathbf{S}\gamma]_\Sigma = 0 \quad \text{on } \Sigma, \quad [\boldsymbol{\nu}\cdot\nabla(\mathbf{S}\gamma)]_\Sigma = \gamma \quad \text{on } \Sigma. \tag{2.3}$$

An important insight (that we outline in appendix A) is the fact that this process can be reversed: in particular, for every eigenfunction φ that solves (2.1) one can find a density γ such that $\varphi(\boldsymbol{x}) = (\mathbf{S}\gamma)(\boldsymbol{x})$. This allows us to substitute the representation $\varphi = \mathbf{S}\gamma$ into the last equation of (2.1),

$$\lambda\gamma(\boldsymbol{x}) = \Delta_T(\mathbf{S}\gamma)(\boldsymbol{x}) \quad \text{on } \Sigma.$$

Let S denote the single-layer operator $\mathbf{S}$ restricted to Σ and set $\xi = S\gamma$. Provided that the inverses S^{-1} and Δ_T^{-1} exist we can further rearrange the eigenvalue problem (2.1) into an equivalent spectral problem,

$$\Delta_T^{-1}S^{-1}\xi = \lambda^{-1}\xi. \tag{2.4}$$

We establish in appendix A that for the case of closed surfaces Σ both inverses S^{-1} and Δ_T^{-1} do indeed exist and that the operator $\Delta_T^{-1}S^{-1}$ is compact and self-adjoint on a modified Hilbert space

$$N(\Sigma) := \left\{\xi \in H^1(\Sigma) : \int_\Sigma S^{-1}\xi \,\mathrm{d}o_x = 0\right\},$$

with associated norm $||\nabla_T \cdot ||_{L^2(\Sigma)}$. Here, $H^1(\Sigma)$ denotes the Sobolev space of square-integrable functions with square-integrable generalized derivatives. In summary, this guarantees the existence of a countable set of real eigenvalues $\{\lambda_n^{-1}\}$, $n = 1, 2, \ldots$ converging to zero, and an associated orthonormal basis of eigenvectors $\{\xi_n\}$ of $N(\Sigma)$. Note that by design ξ_n is precisely the restriction of φ_n, as characterized by (2.1) to the surface Σ.

(b) Spectral characterization of the corrector

Consider now the Y-periodic corrector field $\chi(\boldsymbol{x})$, described by the cell problem (1.2). The aforementioned orthonormal basis of eigenvectors $\{\xi_n\}$ admits (up to a constant) a representation

$$\chi_j(\boldsymbol{x}) = \sum_{n=1}^{\infty} \alpha_j^n \xi_n(\boldsymbol{x}) \quad \text{on } \Sigma.$$

Substituting this characterization back into (1.2) and a bit of algebra exploiting (2.4) then yields an explicit formula for the coefficients,

$$\alpha_j^n = \frac{\lambda_n\eta(\omega)}{\varepsilon - \lambda_n\eta(\omega)} \int_\Sigma P_T(\boldsymbol{e}_j)\cdot\nabla_T\overline{\xi}_n \,\mathrm{d}o_x, \quad \eta(\omega) := \frac{\sigma(\omega)}{\mathrm{i}\omega}, \quad j = 1,2,3. \tag{2.5}$$

Similarly, repeating the substitution for equation (1.2) yields an explicit formula for the frequency behaviour of the effective dielectric tensor,

$$\varepsilon_{ij}^{\mathrm{eff}}(\omega) = \varepsilon\,\delta_{ij} - \eta(\omega)\int_\Sigma P_T(\boldsymbol{e}_j)\cdot P_T(\boldsymbol{e}_i)\,\mathrm{d}o_x - \sum_{n=1}^{\infty}\frac{\lambda_n\,\eta^2(\omega)}{\varepsilon - \lambda_n\,\eta(\omega)} M_{jn}\,\overline{M_{in}}, \tag{2.6}$$

where the factors M_{jn} are defined as

$$M_{jn} = \int_\Sigma P_T(\boldsymbol{e}_j)\cdot\nabla_T\overline{\varphi}_n(\boldsymbol{x})\,\mathrm{d}o_x, \quad j = 1,2,3,\ n = 1,2,\ldots.$$

A number of remarks are in order. Equation (2.6) separates the frequency dependence of the surface conductivity (included in $\eta(\omega)$) from the fundamental (frequency-independent) geometric resonances described by eigenvalue problem (2.1) that determine eigenvalues λ_k and eigenmodes ξ_k. This implies that material properties and geometric resonances, which both contribute to the

frequency response of the effective permittivity tensor $\varepsilon_{ij}^{\text{eff}}(\omega)$, are decoupled: the spectrum λ_k and eigenmodes ξ_k of (2.1) only depend on the (nanoscale) geometry and not on the concrete surface conductivity model.

3. Macroscale frequency response

We now investigate the effective permittivity tensor $\varepsilon^{\text{eff}}(\omega)$ given by (2.6) further. First, the somewhat hidden Lorentz resonance structure in the coefficients of the sum in equation (2.6) is made explicit. We then discuss how equation (2.6) can be used to facilitate the inverse design process [29,30].

(a) Lorentz dispersive material

From (2.6) we see that resonances in the temporal behaviour of the tensor emerge whenever the denominator in the coefficients of the sum is close to zero. Equating the real part of the denominator of

$$\frac{\lambda_n \eta^2(\omega)}{\varepsilon - \lambda_n \eta(\omega)}$$

to zero recovers a critical frequency

$$\omega_{0,n}^2 = \frac{\lambda_n \omega_p}{\varepsilon}. \tag{3.1}$$

Here, we assumed a simple Drude model $\sigma(\omega) = \mathrm{i}\omega_p/(\omega + \mathrm{i}/\tau)$ to hold, where $\omega_p \approx 4/137$ is a rescaled Drude weight and τ is a material-dependent relaxation time. With this definition in place, we can further manipulate the coefficients,

$$\frac{\lambda_n \eta^2(\omega)}{\varepsilon - \lambda_n \eta(\omega)} = \frac{\omega_{0,n}^2 \omega_p}{\omega(\omega + \mathrm{i}/\tau)} \cdot \frac{1}{\omega^2 - \omega_{0,n}^2 + \mathrm{i}\omega/\tau}.$$

In general, the angular frequency ω is much larger than the inverse of the relaxation time, namely $\omega \gg 1/\tau$. Thus, close to resonance we can reasonably assume that $\omega \approx \omega + \mathrm{i}/\tau \approx \omega_{0,n}$ and obtain

$$\frac{\lambda_n \eta^2(\omega)}{\varepsilon - \lambda_n \eta(\omega)} \approx \omega_p \frac{1}{\omega^2 - \omega_{0,n}^2 + \mathrm{i}\omega/\tau} = -\omega_p \frac{\left(\omega_{0,n}^2 - \omega^2\right) - \mathrm{i}\omega/\tau}{\left(\omega_{0,n}^2 - \omega^2\right)^2 + \omega^2/\tau^2}.$$

The coefficients are thus Lorentzian with resonance frequency

$$\omega_{R,n} = \sqrt{\omega_{0,n}^2 - 1/(2\tau)^2}, \quad n = 1, 2, \ldots. \tag{3.2}$$

In summary, we obtain that, up to a constant,

$$\varepsilon_{ij}^{\text{eff}}(\omega) \sim M_{jn}\overline{M_{in}}\, \omega_p \frac{\left(\omega_{0,n}^2 - \omega^2\right) - \mathrm{i}\omega/\tau}{\left(\omega_{0,n}^2 - \omega^2\right)^2 + \omega^2/\tau^2}, \quad \text{for } \omega \approx \omega_{R,n}.$$

We point out that the nanoscale geometry that determines the spectrum λ_n and eigenmodes ξ_n only influences the numerical values of the resonance frequencies $\omega_{0,n}$ and $\omega_{R,n}$ as well as the numerical values of the weights M_{in}.

In summary, this heuristic argument suggests that the macroscale optical response of the plasmonic crystal is that of a *Lorentz dispersive material* [31–33]: the frequency response of the effective permittivity, $\varepsilon^{\text{eff}}(\omega)$, can be approximated by a finite sum of Lorentz resonances, with explicit formulae for resonant frequencies and coefficients provided by our characterization (2.6).

(b) Inverse optical design

The rational expression for the effective property given by (2.6) lends itself to an inverse optimal design paradigm for a desired dispersive response. Equation (2.6) shows that the locations of the poles and zeros are controlled by the eigenvalues λ_n and eigenfunctions ζ_n. These depend on

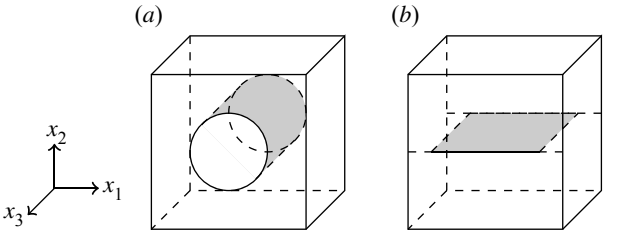

Figure 2. Prototypical geometries: (*a*) a nanotube configuration and (*b*) a nanoribbon configuration. The diameter (in (*a*)) and the width (in (*b*)) was set to 0.8.

the radius of the nanotube or the side length of the nanoribbon. One can compute a library of λ_n and ζ_n near the desired operating frequency for a range of geometric parameters. From this library, one can pick the poles and zeros that deliver the dispersive response closest to the desired one. Here the focus is on manufacturable designs and future studies will investigate libraries of manufacturable geometries to provide a manufacturable range of resonant responses.

4. Computational platform

The spectral decomposition discussed in §2b allows for a very efficient computation of the frequency response of a nanostructure by first solving a single geometric eigenvalue problem given by (2.1) approximately. Then, (2.6) can be invoked to characterize the frequency response of the permittivity tensor. We will illustrate this procedure in this section on two prototypical geometries shown in figure 2: a nanotube configuration, which is a closed smooth surface, and a nanoribbon configuration, which is an open surface with edges. We point out that, because of the translation invariance in the z-direction of both configurations, the corresponding corrector $\boldsymbol{\chi}_3$ vanishes. This implies that the corresponding cell problems (A 1) reduce to a two-dimensional problem, and that the third diagonal component of the effective conductivity tensor ε^{eff} is simply given by

$$\varepsilon_{33}^{\text{eff}} = \varepsilon - \eta(\omega) \int_{\Sigma} 1 \, \mathrm{d}o_x.$$

Owing to symmetry we have $\varepsilon_{11}^{\text{eff}} = \varepsilon_{22}^{\text{eff}}$ for the nanotube configuration. In case of the nanoribbon geometry the averaging process in the y-direction is trivial, leading to $\varepsilon_{22}^{\text{eff}} = \varepsilon$. We thus only need to determine $\varepsilon_{11}^{\text{eff}}$ computationally in the following.

(a) Numerical computation of the geometric spectrum

In order to approximate (2.4) numerically, we recast the eigenvalue problem (2.1) into variational form: find $\varphi_n \in \mathcal{H}$ and $\lambda_n \in \mathbb{R}$ such that

$$\lambda_n \int_Y \nabla\varphi_n(\boldsymbol{x}) \cdot \nabla\overline{\psi}(\boldsymbol{x}) \, \mathrm{d}x = \int_{\Sigma} \nabla_T\varphi_n(\boldsymbol{x}) \cdot \nabla_T\overline{\psi}(\boldsymbol{x}) \, \mathrm{d}o_x, \quad \forall \psi \in \mathcal{H}.$$

This eigenvalue problem can be efficiently approximated with a finite-element discretization which we will quickly outline. We use the finite-element toolkit deal.II [34,35]. To achieve a good numerical convergence order we use unstructured quadrilateral meshes $\mathcal{T}_h$ for both geometries that are fitted to the curved hypersurface Σ by aligning element boundaries with the hypersurface [36] and discretizing with high-order Lagrange elements. Let $\{\psi_i^h\}_{i\in\{1:\mathcal{N}\}}$ be the nodal basis of the Lagrange ansatz. We can then define the usual stiffness matrix $M = (m_{ij})$

$$m_{ij} = \sum_{Q\in\mathcal{T}_h} \int_Q \nabla\psi_j^h(\boldsymbol{x}) \cdot \nabla\psi_i^h(\boldsymbol{x}) \, \mathrm{d}x.$$

Table 1. Numerically computed spectrum and weight coefficients for the two geometries (figure 2) using the computational approach outlined in §3a. Part (a) shows results for the nanotube configuration. All roots have multiplicity 2; eigenvalues with weight 0 are omitted. Part (b) shows results for the nanoribbon geometry. Here all roots have multiplicity 1.

order k	λ_k	$\lvert\int_\Sigma P_T(\boldsymbol{e}_1)\cdot\nabla_T\overline{\xi}_n\,\mathrm{d}o_x\rvert$	λ_k	$\lvert\int_\Sigma P_T(\boldsymbol{e}_1)\cdot\nabla_T\overline{\xi}_n\,\mathrm{d}o_x\rvert$
(a) nanotubes			(b) nanoribbons	
1	0.5924	1.1158	0.9873	0.8543
2	3.726	0.1077	5.314	0.1811
3	6.289	0.008194	9.283	0.1097
4	8.763	0.003574	13.22	0.07913
5	11.26	0.0002755	17.16	0.06194
6	13.76	0.00008546	25.02	0.04322
7	16.27	0.000009443	28.96	0.03755

The boundary term requires a modification because the trace $\nabla_T\psi_i^h$ is not single-valued and only defined on an individual cell of the mesh. We thus define a matrix $S=(s_{ij})$ by averaging both cell contributions to the gradient

$$s_{ij}=\sum_{Q\in\mathcal{T}_h}\frac{1}{2}\int_{\partial Q}\nabla_T\psi_j^h(\boldsymbol{x})\cdot\nabla_T\psi_i^h(\boldsymbol{x})\,\mathrm{d}o_x.$$

We can then compute an approximate spectrum λ_n^h and discrete eigenfunctions $\xi_n^h=\sum_i\Xi_{n,i}^h\psi_i^h$ by solving the matrix eigenvalue problem

$$(S+bM)\,\Xi_n^h=\tilde{\lambda}_n^h\,M\,\Xi_n^h$$

with an eigenvalue solver, such as SLEPc [37]. Here, $b>0$ is a suitably chosen Moebius parameter. The original eigenvalue is recovered by setting $\lambda_n^h=\tilde{\lambda}_n^h-b$. We briefly comment on one crucial subtlety of this approach. The discrete eigenvectors Ξ_n^h are orthonormal with respect to the inner product $\langle M\,.\,,\,.\,\rangle$ because of the mass matrix M appearing on the right-hand side. This inner product is the discrete analogue of $\int_Y\nabla\,.\,\cdot\nabla\,.\,\mathrm{d}x$ and not the normalization we used in §2. This does not change the computed eigenvalues but has an effect on the surface integrals that have to be computed next; see proposition B.5 and the discussion in appendix B. This can be easily cured by scaling the surface integrals appropriately by $1/\sqrt{\lambda_n^h}$; see equations (2.6) and (B 3). We report numerical results for the two geometries (figure 2) in table 1. The decay rate of the weight coefficients $\lvert\int_\Sigma P_T(\boldsymbol{e}_1)\cdot\nabla_T\overline{\xi}_n\,\mathrm{d}o_x\rvert$ deserves a short discussion. The rapid convergence of the coefficients to zero in the case of nanotubes is owed to the regularity of Σ and the absence of interior edges. The eigenvalues and eigenfunctions of the nanotube geometry can be explicitly computed when the periodic boundary condition on Y is replaced by an infinite domain and the Sommerfeld radiation condition (see appendix C). In this case only the first order, namely $k=1$, has a non-zero contribution to the resonance. The rapid decay of the weight coefficients in our numerical result for the periodic case is qualitatively in agreement with this observation. Owing to the singularities at the corners of the nanoribbon geometry [38], it is not surprising that the decay rate of the weight coefficients is limited.

An nth order numerical approximation of the effective permittivity tensor can be constructed by invoking a discrete counterpart of (2.6),

$$\varepsilon_{11}^{\mathrm{app}}(\omega)=\varepsilon-\eta(\omega)\sum_{Q\in\mathcal{T}_h}\sum_{\partial Q\cap\Sigma}P_T(\boldsymbol{e}_1)\cdot P_T(\boldsymbol{e}_1)\,\mathrm{d}o_x-\sum_{n=1}^{N}\frac{\lambda_n^h\eta^2(\omega)}{\varepsilon-\lambda_n^h\,\eta(\omega)}\left|\sum_{Q\in\mathcal{T}_h}\sum_{\partial Q\cap\Sigma}P_T(\boldsymbol{e}_1)\cdot\nabla_T\xi_n^h\,\mathrm{d}o_x\right|^2. \tag{4.1}$$

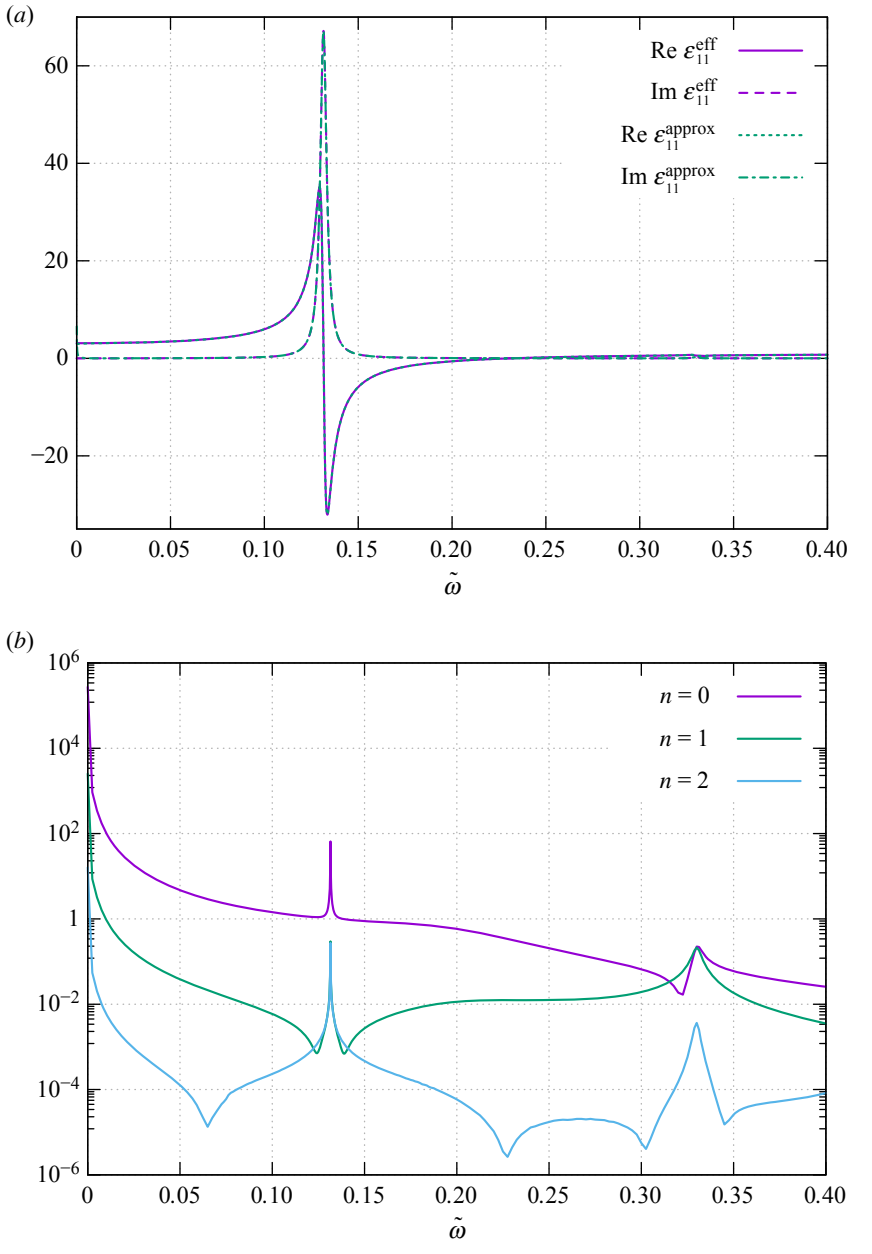

Figure 3. (*a*) Frequency response of $\varepsilon_{ii}^{\text{eff}}(\omega)$, $i = 1, 2$, for the nanotube configuration: the solid (real part) and dashed (imaginary part) lines are computed by solving the cell problem (1.2) for every ω; the dotted and dash-dotted lines are computed by formula (2.6) truncated at $n = 2$. (*b*) The corresponding relative error as a function of frequency. (Online version in colour.)

(b) Comparison

Choosing $\varepsilon = 1$, we compute a reference frequency response of $\varepsilon_{11}^{\text{eff}}(\omega)$ by finely sampling over a set frequency range $0 < \omega < 0.5$ and performing a complete direct numerical computation of the cell problem for selected frequencies: for every chosen angular frequency ω, we first determine the corrector by solving (1.2) with a finite-element code [10] up to a suitable resolution (about 110 000 unknowns for the nanotube configuration and about 130 000 unknowns for the nanoribbon

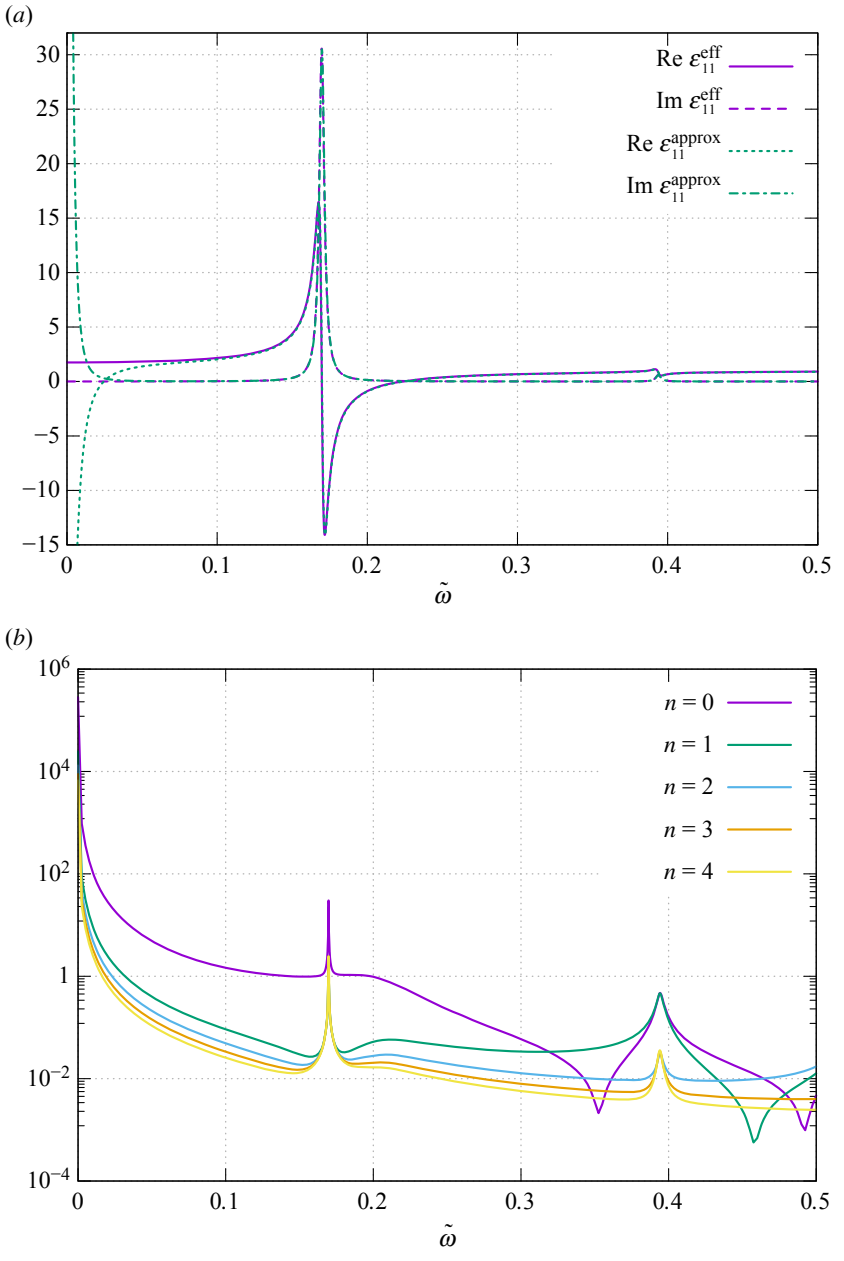

Figure 4. (*a*) Frequency response of $\varepsilon_{11}^{\text{eff}}(\omega)$ for the nanoribbon configuration: the solid (real part) and dashed (imaginary part) lines are computed by solving the cell problem (1.2) for every ω; the dotted and dash-dotted lines are computed by formula (2.6) truncated at $n = 2$. (*b*) The corresponding relative error as a function of frequency. (Online version in colour.)

configuration). The result is plotted in figures 3*a* and 4*a*. In both plots, about 700 frequencies were chosen adaptively.

We then compare a second-order approximation $\varepsilon_{11}^{\text{app}}$ by using (4.1) with $n = 2$ against the direct numerical computation graphically in figures 3*a* and 4*a*. For the chosen frequency range, we observe an excellent agreement of the approximate permittivity $\varepsilon_{11}^{\text{app}}$ with the reference computation in the 'eyeball' norm.

A more detailed comparison of the frequency behaviour of the relative error between both computations is given in figures 3*b* and 4*b*, where also the dependence of the error on the order n

of the approximation (4.1) is visualized. On average we observe a relative error of less than 1%. We note that the maxima in the relative error naturally occur at corresponding Lorentz resonances and are dominated by the approximation error of the underlying finite-element simulations. We observe an exponential decay of the relative error as a function of the approximation order for the smooth nanotube geometry (figure 3*b*). The corresponding convergence behaviour for nanoribbons as shown in figure 4*b* is significantly slower. This is owed to the fact that the edges in the nanoribbon geometry cause singularity in the solution of the cell problems, thus limiting the approximation order [38].

5. Conclusion

In this paper, we analysed the Lorentz resonances in plasmonic crystals that consist of two-dimensional nano-dielectric inclusions embedded in a non-magnetic bulk. From the corrector field found in a rigorous homogenization theory (A 1), we derived an analytic expansion formula for the effective permittivity (1.3). This formula decouples the local geometric resonances and the material properties, and thus enables a very efficient approximation to compute the frequency response. This formula holds for inclusions of a large family of geometries, including closed surfaces (as shown in §2 and appendix A) and open surfaces that can be completed into closed surfaces as shown in appendix B.

We observe that, up to a constant factor, the nth Lorentz resonance is described by

$$\frac{\lambda_n \eta^2(\omega)}{\varepsilon - \lambda_n \eta(\omega)} \approx \omega_p \frac{1}{\omega^2 - \omega_{0,n}^2 + \mathrm{i}\omega/\tau} = -\omega_p \frac{(\omega_{0,n}^2 - \omega^2) + \mathrm{i}\omega/\tau}{(\omega_{0,n}^2 - \omega^2)^2 + \omega^2/\tau^2}.$$

We have also observed that a crucial quantity that determines the convergence speed of this expansion is the decay rate of a weight factor

$$|M_{jn}| = \left| \int_\Sigma P_T(\boldsymbol{e}_j) \cdot \nabla_T \overline{\xi}_n \, \mathrm{d}o_x \right|^2.$$

The decay rate depends on the smoothness of the corrector, i.e. whether singularities due to roughness or edges are present in the cell problem. We have demonstrated that our spectral decomposition approach offers a significant saving in computational resources because only one frequency-independent geometric eigenvalue problem has to be computed, in contrast to computing the corrector field for a huge number of fixed frequencies.

Data accessibility. Source code and configuration files of all computations have been made available at https://github.com/tamiko/rspa-2021 and https://zenodo.org/record/5610286#.YXvH957MJ9M.

Authors' contributions. W.L., R.L. and M.M. contributed to the conception, design and analysis of the mathematical model. M.M. developed the code. W.L., R.L. and M.M. designed the numerical tests. M.M. performed the numerical simulation. All authors critically discussed the numerical results. All authors contributed to writing and editing the paper.

Competing interests. We declare we have no competing interests.

Funding. R.L. acknowledges partial support by the NSF under grant nos. DMS-1921707 and DMS-1813698; M.M. acknowledges partial support by the NSF under grant nos. DMS-1912847 and DMS-2045636.

Appendix A. Spectral decomposition for closed surfaces

We now give a rigorous mathematical proof of the spectral decomposition introduced in §2 through the use of a weak formulation. The mathematical proof involves simpler function spaces when the surface Σ is closed. For this reason, we first discuss the case of a closed surface and discuss the case of open surfaces based on the notion of fractional Sobolev spaces in appendix B.

(a) The weak formulation

Provided the surface Σ is Lipschitz continuous (implying that it admits a uniquely defined surface normal), the Y-periodic corrector field $\boldsymbol{\chi}(\boldsymbol{x})$ is the solution of the variational *cell problem* [6],

$$\mathrm{i}\omega\varepsilon \int_Y \nabla\chi_j(\omega,\boldsymbol{x})\cdot\nabla\overline{\psi(\boldsymbol{x})}\,\mathrm{d}x - \sigma(\omega)\int_\Sigma \nabla_T\chi_j(\omega,\boldsymbol{x})\cdot\nabla_T\overline{\psi(\boldsymbol{x})}\,\mathrm{d}o_x = \sigma(\omega)\int_\Sigma P_T(\boldsymbol{e}_j)\cdot\nabla_T\overline{\psi(\boldsymbol{x})}\,\mathrm{d}o_x. \quad (A\,1)$$

The appropriate function space for the variational problem (A 1) is

$$\mathcal{H} := \left\{\psi \in H^1_{\mathrm{per}}(Y,\mathbb{C}) : \nabla_T\psi \in L^2(\Sigma,\mathbb{C}),\ \int_Y \psi = 0\right\}. \quad (A\,2)$$

Here, $H^1_{\mathrm{per}}(Y)$ denotes the Sobolev space of periodic functions u such that u and its first-order (distributional) partial derivatives are square integrable in Y, and $L^2(\Sigma)$ denotes the space of square-integrable functions on Σ. The space $\mathcal{H}$ equipped with the norm

$$||\cdot||^2_{\mathcal{H}} = ||\nabla\cdot||^2_Y + ||\nabla_T\cdot||^2_\Sigma$$

(and the corresponding inner product) is a Hilbert space. It can be shown that the corrector problem (A 1) admits a unique solution $\chi_j \in \mathcal{H}$ [5–9].

Thus, the auxiliary spectral problem partitioning between the first two integrals in (A 1), parallel to (2.1), is to find all pairs of eigenfunctions $\varphi \in \mathcal{H}$ and eigenvalues $\lambda \in \mathbb{R}$, such that

$$\lambda\int_Y \nabla\varphi\cdot\nabla\overline{\psi}\,\mathrm{d}x = \int_\Sigma \nabla_T\varphi\cdot\nabla_T\overline{\psi}\,\mathrm{d}o_x \quad \text{for all } \psi\in\mathcal{H}. \quad (A\,3)$$

(b) A density representation for the corrector

The corrector $\chi_i \in \mathcal{H}$ given by (A 1) can be characterized in terms of the Y-periodic single-layer potential $\mathbf{S}$ (2.2) with a density γ. Recall that we have restricted the discussion to the case of Σ without internal edges in Y. In this case, the following two properties hold:

(i) The restricted single-layer operator $S : L^2(\Sigma) \to H^1(\Sigma)$ defined by (2.3) is a bounded, invertible operator with a bounded inverse.
(ii) The jump in the normal derivative of the solution $\chi_i \in \mathcal{H}$ of the cell problem (A 1) on the surface, $[\partial_\nu\chi_j]_\Sigma$, is in $L^2(\Sigma)$, where $L^2(\Sigma)$ is the space of square-integrable functions on Σ.

A proof of (i) for the case of Lipschitz continuous Σ can be found in [39, theorem 7.17], and property (ii) is a direct consequence of the standard trace theorems [40] and property (i). Note that properties (i) and (ii) do not hold when Σ is an open surface (i.e. when Σ has edges in the interior of Y; see appendix B). Starting from (ii), we set

$$\gamma := [\partial_\nu\chi_j] \in L^2(\Sigma,\mathbb{C}).$$

Recalling (2.3) we observe that the difference $\chi_j - \mathbf{S}\gamma$ belongs to $H^1_{\mathrm{per}}(Y,\mathbb{C})$ and its distributional Laplacian is zero everywhere in Y. Therefore,

$$\chi_j = \mathbf{S}\gamma + C,$$

where C is a constant. This suggests the following lemma.

Lemma A.1. *For the corrector χ_j solving (A 1), there exists a unique $\gamma \in L^2(\Sigma,\mathbb{C})$ and a unique complex valued constant C, such that*

$$\chi_j = S\gamma + C, \quad \textit{with} \int_\Sigma \gamma\,\mathrm{d}o_x = 0. \quad (A\,4)$$

Proof. We have already established its existence. For the uniqueness, assume that we have two representations for χ_j, namely $\mathbf{S}\gamma_1 + C_1 = \mathbf{S}\gamma_2 + C_2$. This implies that $\mathbf{S}(\gamma_1 - \gamma_2)$ is a constant in Y, and thus

$$\gamma_1 - \gamma_2 = [\partial_{\boldsymbol{\nu}} \mathbf{S}(\gamma_1 - \gamma_2)] = 0 \quad \text{on } \Sigma.$$

It follows that C_1 and C_2 are also identical. Finally, note that $\Delta \mathbf{S}\gamma = 0$ implies

$$\int_\Sigma \gamma \, \mathrm{d}o_x = \int_\Sigma [\partial_{\boldsymbol{\nu}} \mathbf{S}\gamma] \, \mathrm{d}o_x = -\int_{Y\setminus\Sigma} \Delta \mathbf{S}\gamma \, \mathrm{d}x = 0. \tag{A 5}$$

■

(c) An equivalent spectral problem and symmetrization

Using the same argument again as in the preceding subsection (appendix Ab), for closed Σ every eigenfunction φ of the spectral problem (A 3) has a representation $\varphi = \mathbf{S}\gamma$, where $\gamma \in L^2(\Sigma)$. Substituting the representation $\varphi = \mathbf{S}\gamma$ into (A 3), we obtain an equivalent spectral problem for γ,

$$\lambda \int_Y \nabla \mathbf{S}\gamma \cdot \nabla \overline{\psi} \, \mathrm{d}x = \int_\Sigma \nabla_T \mathbf{S}\gamma \cdot \nabla_T \overline{\psi} \, \mathrm{d}o_x, \quad \text{for all } \psi \in \mathcal{H}.$$

Integration by parts of the volume integral and (2.3) further transforms the eigenvalue problem to an eigenvalue problem described exclusively on Σ,

$$-\lambda \int_\Sigma \gamma \, \overline{\psi} \, \mathrm{d}o_x = \int_\Sigma \nabla_T S\gamma \cdot \nabla_T \overline{\psi} \, \mathrm{d}o_x \quad \text{for all } \psi \in \mathcal{H}.$$

Writing $\xi = S\gamma$, which is equivalent to $\gamma = S^{-1}\xi$ since $S : L^2(\Sigma) \to H^1(\Sigma)$ is invertible for closed Σ, we obtain

$$-\lambda \int_\Sigma S^{-1}\xi \, \overline{\psi} \, \mathrm{d}o_x = \int_\Sigma \nabla_T \xi \cdot \nabla_T \overline{\psi} \, \mathrm{d}o_x, \quad \forall \, \psi \in \mathcal{H}.$$

(d) A compact and self-adjoint operator

The property of the density function γ in lemma A.1 suggests that we work with the space

$$N(\Sigma) := \left\{ \xi \in H^1(\Sigma) : \int_\Sigma S^{-1}\xi \, \mathrm{d}o_x = 0 \right\}. \tag{A 6}$$

A straightforward calculation shows that $N(\Sigma)$ equipped with the norm $||\nabla_T \xi||_{L^2(\Sigma)}$ is a Hilbert space. The Riesz representation theorem then establishes a particular inverse of the Laplace–Beltrami operator Δ_T.

Lemma A.2. *For $f \in L^2(\Sigma)$ with $\int_\Sigma f \, \mathrm{d}o_x = 0$, there exists a unique $g \in N(\Sigma)$, such that*

$$\int_\Sigma \nabla_T g \cdot \nabla_T \overline{\psi} \, \mathrm{d}o_x = -\int_\Sigma f \overline{\psi} \, \mathrm{d}o_x, \quad \textit{for all } \psi \in N(\Sigma).$$

Moreover, the solution g is bounded, namely $||\nabla_T g||_{L^2(\Sigma)} \le C||f||_{L^2(\Sigma)}$. We will denote this solution operator by Δ_T^{-1}.

We are now in a position to formulate and prove a central proposition and corollary.

Proposition A.3. *The operator*

$$\Delta_T^{-1} S^{-1} : N(\Sigma) \to N(\Sigma)$$

is compact and self-adjoint. Moreover, ker $(\Delta_T^{-1} S^{-1}) = \{0\}$.

Corollary A.4 (Spectrum). *The spectrum of $\Delta_T^{-1} S^{-1}$ consists of countably many non-zero eigenvalues $\{\lambda_n^{-1}\}_n$, only possibly accumulating at 0. The corresponding eigenfunctions $\{\xi_n\}$ form an orthonormal basis of $N(\Sigma)$.*

Proof of proposition A.3. $\Delta_T^{-1}S^{-1}$ is well defined and bounded by virtue of property (i) and lemma A.2. For any given $f, g \in N(\Sigma)$, it holds that

$$-\int_\Sigma \left(\nabla_T\, \Delta_T^{-1}S^{-1}f\right)\cdot \nabla_T g \,\mathrm{d}o_x = \int_\Sigma \left(S^{-1}f\right)g \,\mathrm{d}o_x = \int_\Sigma f\left(S^{-1}g\right)\mathrm{d}o_x$$
$$= -\int_\Sigma \nabla_T f \cdot \left(\nabla_T\, \Delta_T^{-1}S^{-1}g\right)\mathrm{d}o_x.$$

Therefore, $\Delta_T^{-1}S^{-1}$ is self-adjoint.

In order to establish the compactness of $\Delta_T^{-1}S^{-1}$, we first fix a bounded sequence $g_i \in N(\Sigma)$. The image $u_i = \Delta_T^{-1}S^{-1}g_i$ is also a bounded sequence in $N(\Sigma)$. By Rellich's lemma, there exists subsequence u_{i_k} that is convergent in $L^2(\Sigma)$. Furthermore, we have

$$\int_\Sigma \nabla_T u_i \cdot \nabla_T u_j \,\mathrm{d}o_x = -\int_\Sigma S^{-1}g_i\, u_j \,\mathrm{d}o_x.$$

Thus $\nabla_T u_{i_k}$ converges componentwise in $L^2(\Sigma)$, which gives that u_{i_k} converges in $N(\Sigma)$.

The last statement follows immediately from the fact that S and Δ_T are bounded and invertible. Thus $\Delta_T^{-1}S^{-1}f \equiv 0$ immediately implies $f \equiv S\ \Delta_T 0 = 0$. ∎

(e) Proof of the spectral decomposition result

Proof of (2.6). Let χ_j be the solution of (A 1). According to lemma A.1, we can write χ_j as a single-layer potential with a density $\gamma \in L^2(\Sigma)$ that satisfies $\int_\Sigma \gamma \,\mathrm{d}o_x = 0$, namely

$$\chi_j = \mathbf{S}\gamma + C.$$

Using the invertibility of S, we obtain that, for $\xi = S\gamma \in N(\Sigma)$,

$$\chi_j = \mathbf{S}\, S^{-1}\xi + C.$$

Corollary A.4 guarantees the existence of the expansion $\xi = \sum_k \alpha_j^k \xi_k$ with $\{\alpha_j^n\}_n \in \ell^2(\mathbb{C})$, which yields (up to a constant)

$$\chi_j = \mathbf{S}S^{-1}\left(\sum_k \alpha_j^k \xi_k\right).$$

Identity (2.5) follows directly from substituting this expansion into (A 1) and testing with $\psi = \mathbf{S}S^{-1}\xi_k$,

$$\eta(\omega)\int_\Sigma P_T(\boldsymbol{e}_j)\cdot\nabla_T\overline{\xi_k}\,\mathrm{d}o_x = \sum_n (\varepsilon\alpha_j^n/\lambda_n - \alpha_j^n\eta(\omega))\int_\Sigma \nabla_T\xi_n\cdot\nabla_T\overline{\xi_k}\,\mathrm{d}o_x$$
$$= \sum_n (\varepsilon\alpha_j^n/\lambda_n - \alpha_j^n\eta(\omega))\,\delta_{kn}$$
$$= \varepsilon\alpha_j^k/\lambda_k - \alpha_j^k\eta(\omega).$$

Finally, identity (2.6) follows from a similar substitution using equations (2.5) and (1.1). ∎

Appendix B. Spectral decomposition on open surfaces

When Σ is an open surface, in the sense that Σ has edges in the interior of Y, the property in §2b, $S : L^2(\Sigma) \to H^1(\Sigma)$ is invertible, no longer holds. A counter-example is the fact that, in two-dimensional space, the non-periodic single-layer potential maps $1/\sqrt{a-x^2}$ to a constant function on the interval $[-a, a]$ [41]. This means that we cannot write $\chi_j = \mathbf{S}\gamma + C$ for some $\gamma \in L^2(\Sigma)$. However, this representation is valid for γ defined in a proper *fractional* Sobolev space. Thus, modifying the argument to fractional Sobolev spaces makes it possible to obtain the same expansion (2.6).

In this appendix, we collect all necessary modifications to the argument outlined in appendix A, provided that the mild assumptions hold true that Σ has a smooth boundary and Σ can be completed into a closed smooth surface Σ_*.

(a) Sobolev spaces on open surfaces

We give a definition of Sobolev spaces defined on open surfaces following the notations in [39]. First, on a closed $C^{k,1}$ surface Σ_* in $\mathbb{R}^n$, where $k \geq 0$ and $n > 0$ are integers, $H^s(\Sigma_*)$ is defined through charts and the Fourier transform for $s \in [-k-1, k+1]$ [39, p. 98].

Let Σ be an open subset of Σ_* and, for simplicity, assume that the boundary of Σ is smooth. For every real number $s \in \mathbb{R}$, we define

$$H^s(\Sigma) := \{f : \Sigma \to \mathbb{C} | f \text{ has an extension } \tilde{f} \in H^s(\Sigma_*)\}$$

$$\tilde{H}^s(\Sigma) := \text{closure of } C_0^\infty(\Sigma) \quad \text{in } H^s(\Sigma_*).$$

It is shown in [39, theorems 3.14, 3.29, 3.30] that when Σ is a Lipschitz subset of Σ_*, for all $s \in \mathbb{R}$,

$$(\tilde{H}^s(\Sigma))' = H^{-s}(\Sigma),$$

$$(H^s(\Sigma))' = \tilde{H}^{-s}(\Sigma)$$

and

$$\tilde{H}^s(\Sigma) = \{f \in H^s(\Sigma_*) | \text{supp} f \subset \overline{\Sigma}\},$$

and, for an integer $m \in [0, k+1]$,

$$H^m(\Sigma) = \{f : \Sigma \to \mathbb{C} | f \text{ and its weak tangential derivatives up to order } m \text{ are in } L^2(\Sigma)\}.$$

Note that the above defined $H^s(\Sigma)$ and $\tilde{H}^{-s}(\Sigma)$ for $s \geq 0$ are the same as those defined in [42,43].

(b) Spectral decomposition

We can now modify the argument in appendix A as follows. Since χ_j belongs to $H^1(Y)$, its distributional Laplacian is 0 and $[\partial_n \chi_j] = 0$ on $\Sigma_* \backslash \Sigma$, so we obtain the standard result shown in lemma B.1.

Lemma B.1. *For the corrector χ_j solving (A 1), there exists a unique $\gamma \in \tilde{H}^{-1/2}(\Sigma, \mathbb{C})$ and a unique constant C, such that*

$$\chi_j = S\gamma + C.$$

This γ satisfies that $\int_\Sigma \gamma \, \mathrm{d}o_x = 0$.

The mapping property of S on $\tilde{H}^{-1/2}(\Sigma)$ is given by lemma B.2.

Lemma B.2 ([42,43]). *The single-layer operator $S : \tilde{H}^{-1/2}(\Sigma) \to H^{1/2}(\Sigma)$ is bijective.*

The proper Hilbert space to consider becomes

$$\mathcal{N}(\Sigma) := \left\{ f \in H^{1/2}(\Sigma), \langle S^{-1} f, 1 \rangle_\Sigma = 0 \right\}, \tag{B 1}$$

equipped with the inner product $\langle -S^{-1}\xi, \eta \rangle_\Sigma$. Here, $\langle \cdot, \cdot \rangle_\Sigma$ is the $L^2(\Sigma)$ pairing, and we will refer to $\langle -S^{-1}\xi, \eta \rangle_\Sigma$ as the S^{-1} inner product.

On this space, we consider the following inverse of Δ_T.

Lemma B.3 (A particular inverse of Δ_T). *For $f \in \tilde{H}^{-1}(\Sigma)$ with $\langle f, 1 \rangle_\Sigma = 0$, there exists a unique $g \in H^1(\Sigma)$ with $\langle S^{-1} g, 1 \rangle_\Sigma = 0$, such that*

$$-\langle f, \psi \rangle_\Sigma = \int_\Sigma \nabla_T g \cdot \nabla_T \overline{\psi} \, \mathrm{d}o_x, \quad \textit{for all } \psi \in H^1(\Sigma). \tag{B 2}$$

Moreover, the solution g of (B2) is bounded, $||g||_{H^1(\Sigma)} \leq C||f||_{H^{-1}(\Sigma)}$. We will denote this solution operator by Δ_T^{-1}.

Proof. Given $f \in \tilde{H}^{-1}(\Sigma)$ with $\langle f, 1\rangle_\Sigma = 0$, it follows from standard elliptic equation theory that there exists a unique $\tilde{g} \in H^1(\Sigma)$ with $\langle \tilde{g}, 1\rangle_\Sigma = 0$, such that

$$-\int_\Sigma f\overline{\psi}\,\mathrm{d}o_x = \int_\Sigma \nabla_T\tilde{g}\cdot\nabla_T\overline{\psi}\,\mathrm{d}o_x \quad \forall\psi \in H^1(\Sigma)$$

and

$$||\tilde{g}||_{H^1(\Sigma)} \le C||f||_{\tilde{H}^{-1}(\Sigma)}.$$

Now let $g_0 = S^{-1}1 \in \tilde{H}^{-1/2}(\Sigma)$ and define the constant

$$C(\tilde{g}) := \frac{\langle S^{-1}\tilde{g}, 1\rangle_\Sigma}{\langle S^{-1}1, 1\rangle_\Sigma} = \frac{\langle \tilde{g}, g_0\rangle_\Sigma}{\langle 1, g_0\rangle_\Sigma}.$$

The function $g := \tilde{g} - C(\tilde{g})$ obviously solves (B 2) and by construction $\langle S^{-1}g, 1\rangle_\Sigma = 0$. The bound follows from

$$||C(\tilde{g})||_{H^1} = ||C(\tilde{g})||_{L^2} \le C|\langle S^{-1}\tilde{g}, 1\rangle| \le C||S^{-1}\tilde{g}||_{L^2} \le C||\tilde{g}||_{H^1} \le C||f||_{\tilde{H}^{-1}}.$$

■

Since $\Delta_T^{-1}S^{-1}$ maps $N(\Sigma) \subset H^{1/2}(\Sigma)$ into $H^1(\Sigma) \subset\subset H^{1/2}(\Sigma)$, we can verify the following.

Proposition B.4. *The operator*

$$\Delta_T^{-1}S^{-1} : \mathcal{N}(\Sigma) \to \mathcal{N}(\Sigma)$$

is compact and self-adjoint with respect to the S^{-1} pairing. Here Δ_T^{-1} is the particular operator defined in lemma B.3. Moreover,

$$ker\,(\Delta_T^{-1}S^{-1}) = \{0\}.$$

Finally, the main result reads as follows.

Proposition B.5 (Spectral decomposition for open surfaces). *Let χ_j be the solution of the cell problem* (A 1). *Let $\{\xi_n, \lambda_n^{-1}\}_n$ be the orthonormal eigensystem of the operator $\Delta_T S$ in the space $\mathcal{N}(\Sigma)$. Then*

$$\chi_j = SS^{-1}\left(\sum_n \alpha_j^n \xi_n\right) + C,$$

where C is a constant and

$$\alpha_j^n = \frac{\eta(\omega)}{\varepsilon - \lambda_n\,\eta(\omega)}\int_\Sigma P_T(\boldsymbol{e}_j)\cdot\nabla_T\overline{\xi}_k\,\mathrm{d}o_x.$$

Furthermore,

$$\varepsilon_{ij}^{\mathrm{eff}} = \varepsilon\,\delta_{ij} - \eta(\omega)\int_\Sigma P_T(\boldsymbol{e}_j)\cdot P_T(\boldsymbol{e}_i)\,\mathrm{d}o_x - \sum_n \frac{\eta^2(\omega)}{\varepsilon - \lambda_n\,\eta(\omega)}\int_\Sigma P_T(\boldsymbol{e}_j)\cdot\nabla_T\overline{\xi}_n\,\mathrm{d}o_x\int_\Sigma \nabla_T\xi_n\cdot P_T(\boldsymbol{e}_i)\,\mathrm{d}o_x. \tag{B 3}$$

Note that the S^{-1} inner product gives a different normalization of ξ_n and hence different α_j^n values. In terms of the scaled function $\tilde{\xi}_k := \xi_k/\sqrt{|\lambda_k|}$, (2.1) is satisfied and the expansion (B 3) takes the same form as (1.3).

Appendix C. Explicitly computable examples

We explicitly compute the eigensystem of $\Delta_T^{-1}S^{-1}$ on two *non-periodic* geometries in $\mathbb{R}^3$. These examples qualitatively illustrate the corresponding periodic geometries, when the inclusions are far apart from each other. On spheres and circular cylinders in $\mathbb{R}^3$, the eigensystems of $\Delta_T S$ are explicitly known. This is because Δ_T and S separately have explicit eigensystems, and they share

eigenfunctions. Note that the only manifolds on which the Laplace–Beltrami operator has explicit eigensystems are n-spheres, n-tori and Heisenberg groups.

(a) Circular cylinder

Let Σ be a cylinder with a circular cross-section of radius a. The corresponding periodic geometry is the nanotube structure considered numerically in §4. We will abuse notation by denoting the cross-sections of all quantities by the same notation, since all quantities are invariant along the axis of the cylinder. A basis for mean zero $L^2(\Sigma)$ functions is $\{e^{in\theta}, n \neq 0\}$. This is also a set of simultaneous eigenfunctions for Δ_T and S,

$$\Delta_T e^{in\theta} = -\frac{n^2}{a^2} e^{in\theta} \quad \text{and} \quad S e^{in\theta} = -\frac{a}{2n} e^{in\theta}.$$

Thus the eigensystem for (2.4) normalized in the $||\nabla_T \cdot ||_{L^2(\Sigma)}$ norm is

$$\lambda_n = \frac{n}{2a}, \quad \xi_n^k = \begin{cases} \frac{1}{n}\sqrt{\frac{a}{\pi}}\cos(n\theta), & k=1, \\ \frac{1}{n}\sqrt{\frac{a}{\pi}}\sin(n\theta), & k=2, \end{cases} \qquad n \geq 1.$$

Using $P_T(\boldsymbol{e}_1) = -\hat{\theta}\sin\theta$ and $\nabla_T = \hat{\theta}\frac{1}{a}\partial_\theta$, we obtain

$$\int_\Sigma P_T(\boldsymbol{e}_1) \cdot \nabla_T \overline{\xi}_n^k \, do_x = \begin{cases} \sqrt{\pi a}, & n=1,\ k=1, \\ 0, & \text{otherwise.} \end{cases}$$

Note that, for the corresponding periodic geometry, the factor $\int_\Sigma P_T(\boldsymbol{e}_1) \cdot \nabla_T \overline{\xi}_n^k \, do_x$ in table 1 decays, instead of falling to zero abruptly. This is due to the effect from other cylinders in the array. The decay becomes faster when the size of the cylinder relative to the cell becomes smaller.

(b) Sphere

Let Σ be a sphere of radius a. A basis for mean zero $L^2(\Sigma)$ functions is the set of spherical harmonic functions $\{Y_n^m, n \geq 1, -n \leq m \leq n\}$. This is also a set of simultaneous eigenfunctions for Δ_T and S,

$$\Delta_T Y_n^m = -\frac{n(n+1)}{a^2} Y_n^m \quad \text{and} \quad S Y_{n,m} = -\frac{a}{2n+1} Y_{n,m}.$$

Thus the eigensystem for (2.4) normalized in the $||\nabla_T \cdot ||_{L^2(\Sigma)}$ norm is

$$\lambda_n = \frac{n(n+1)}{a(2n+1)}, \quad \xi_n^i = \frac{1}{\sqrt{n(n+1)}} Y_{n,m}, \quad n \geq 1, -n \leq m \leq n.$$

Using $P_T(\boldsymbol{e}_1) = \hat{\theta}\cos\theta\cos\phi - \hat{\phi}\sin\phi$, $\nabla_T = \hat{\theta}(1/a)\partial_\theta + \hat{\phi}(1/a\sin\theta)\partial_\phi$ and the recurrence relations for the associated Legendre polynomials, we obtain

$$\int_\Sigma P_T(\boldsymbol{e}_1) \cdot \nabla_T \overline{\xi}_n^i \, do_x = \begin{cases} \mp 2a\sqrt{\frac{\pi}{3}}, & n=1,\ m=\pm 1, \\ 0, & \text{otherwise.} \end{cases}$$

References

1. Zhao Y, Alù A. 2011 Manipulating light polarization with ultrathin plasmonic metasurfaces. *Phys. Rev. B* **84**, 205428. (doi:10.1103/PhysRevB.84.205428)
2. Zhao Y, Liu X-X, Alù A. 2014 Recent advances on optical metasurfaces. *J. Opt.* **16**, 123001. (doi:10.1088/2040-8978/16/12/123001)

3. Taubert R, Dregely D, Stroucken T, Christ A, Giessen H. 2012 Octave-wide photonic band gap in three-dimensional plasmonic Bragg structures and limitations of radiative coupling. *Nat. Commun.* **3**, 691. (doi:10.1038/ncomms1694)
4. Pors A, Albrektsen O, Radko IP, Bozhevonlnyi SI. 2013 A review of gap-surface plasmon metasurfaces: fundamentals and applications. *Sci. Rep.* **3**, 2155. (doi:10.1038/srep02155)
5. Amirat Y, Shelukhin VV. 2017 Homogenization of time harmonic Maxwell equations: the effect of interfacial currents. *Math. Methods Appl. Sci.* **40**, 3140–3162. (doi:10.1002/mma.4229)
6. Maier M, Margetis D, Mellet A. 2020 Homogenization of time-harmonic Maxwell's equations in nonhomogeneous plasmonic structures. *J. Comput. Appl. Math.* **377**, 112909. (doi:10.1016/j.cam.2020.112909)
7. Wellander N. 2001 Homogenization of the Maxwell equations: case I. Linear theory. *Appl. Math.* **46**, 29–51. (doi:10.1023/A:1013727504393)
8. Wellander N. 2002 Homogenization of the Maxwell equations: case II. Nonlinear conductivity. *Appl. Math.* **47**, 255–283. (doi:10.1023/A:1021797505024)
9. Wellander N, Kristensson G. 2003 Homogenization of the Maxwell equations at fixed frequency. *SIAM J. Appl. Math.* **64**, 170–195. (doi:10.1137/S0036139902403366)
10. Maier M, Mattheakis M, Kaxiras E, Luskin M, Margetis D. 2019 Homogenization of plasmonic crystals: seeking the epsilon-near-zero effect. *Proc. R. Soc. A* **475**, 20190220. (doi:10.1098/rspa.2019.0220)
11. Maier M, Margetis D, Luskin M. 2020 Finite-size effects in wave transmission through plasmonic crystals: a tale of two scales. *Phys. Rev. B* **102**, 075308. (doi:10.1103/PhysRevB.102.075308)
12. Chen Y, Lipton R. 2013 Resonance and double negative behavior in metamaterials. *Arch. Ration. Mech. Anal.* **209**, 835–868. (doi:10.1007/s00205-013-0634-8)
13. Mattheakis M, Valagiannopoulos CA, Kaxiras E. 2016 Epsilon-near-zero behavior from plasmonic Dirac point: theory and realization using two-dimensional materials. *Phys. Rev. B* **94**, 201404(R). (doi:10.1103/PhysRevB.94.201404)
14. Moitra P, Yang Y, Anderson Z, Kravchenko II, Briggs DP, Valentine J. 2013 Realization of an all-dielectric zero-index optical metamaterial. *Nat. Photonics* **7**, 791–795. (doi:10.1038/nphoton.2013.214)
15. Niu X, Hu X, Chu S, Gong Q. 2018 Epsilon-near-zero photonics: a new platform for integrated devices. *Adv. Opt. Mater.* **6**, 1701292. (doi:10.1002/adom.201701292)
16. Silveirinha M, Engheta N. 2006 Tunneling of electromagnetic energy through subwavelength channels and bends using epsilon-near-zero materials. *Phys. Rev. Lett.* **97**, 157403. (doi:10.1103/PhysRevLett.97.157403)
17. Tan T, Jiang X, Wang C, Yao B, Zhang H. 2020 2D material optoelectronics for information functional device applications: status and challenges. *Adv. Sci.* **7**, 2000058. (doi:10.1002/advs.202000058)
18. Xia F, Wang H, Xiao D, Dubey M, Ramasubramaniam A. 2014 Two-dimensional material nanophotonics. *Nat. Photonics* **8**, 899–907. (doi:10.1038/nphoton.2014.271)
19. Wintz D, Genevet P, Ambrosio A, Woolf A, Capasso F. 2015 Holographic metalens for switchable focusing of surface plasmons. *Nano Lett.* **15**, 3585–3589. (doi:10.1021/acs.nanolett.5b01076)
20. Nemilentsau A, Low T, Hanson G. 2016 Anisotropic 2D materials for tunable hyperbolic plasmonics. *Phys. Rev. Lett.* **116**, 066804. (doi:10.1103/PhysRevLett.116.066804)
21. Alù A, Engheta N. 2005 Achieving transparency with plasmonic and metamaterial coatings. *Phys. Rev. E* **72**, 016623. (doi:10.1103/PhysRevE.72.016623)
22. Cheng J, Wang WL, Mosallaei H, Kaxiras E. 2014 Surface plasmon engineering in graphene functionalized with organic molecules: a multiscale theoretical investigation. *Nano Lett.* **14**, 50–56. (doi:10.1021/nl403005s)
23. Bergman DJ. 1978 The dielectric constant of a composite material—a problem in classical physics. *Phys. Rep.* **43**, 377–407. (doi:10.1016/0370-1573(78)90009-1)
24. McPhedran RC, Milton GW. 1981 Bounds and exact theories for transport properties of inhomogeneous media. *Appl. Phys. A* **26**, 207–220. (doi:10.1007/BF00617840)
25. Golden K, Papanicolaou G. 1983 Bounds for effective parameters of heterogeneous media by analytic continuation. *Commun. Math. Phys.* **90**, 473–491. (doi:10.1007/BF01216179)
26. Milton GW. 1981 Bounds on the complex permittivity of a two-component composite material. *J. Appl. Phys.* **52**, 5286–5293. (doi:10.1063/1.329385)

27. Milton GW. 2002 *The theory of composites*. Cambridge, UK: Cambridge University Press.
28. Lipton R, Viator R. 2017 Bloch waves in crystals and periodic high contrast media. *ESAIM Math. Model. Numer. Anal.* **51**, 889–918. (doi:10.1051/m2an/2016046)
29. Miller OD, Yablonovitch E. 2015 Inverse optical design. In *Encyclopedia of applied and computational mathematics* (ed. B Engquist), pp. 729–732. Berlin, Germany: Springer.
30. Molesky S, Lin Z, Piggott AY, Jin W, Vucković J, Rodriguez AW. 2018 Inverse design in nanophotonics. *Nat. Photonics* **12**, 659–670. (doi:10.1038/s41566-018-0246-9)
31. Born M, Wolf E. 2013 *Principles of optics: electromagnetic theory of propagation, interference and diffraction of light*, 6th corrected edn. Amsterdam, The Netherlands: Elsevier.
32. Kittel C. 2005 *Introduction to solid state physics*, 8th edn. Hoboken, NJ: John Wiley and Sons, Inc.
33. Lorentz HA. 1916 *The theory of electrons and its applications to the phenomena of light and radiant heat*, vol. 29. New York, NY: GE Stechert & Company.
34. Arndt D *et al.* 2020 The deal.II library, version 9.2. *J. Numer. Math.* **28**, 131–146. (doi:10.1515/jnma-2020-0043)
35. Arndt D *et al.* 2021 The deal.II finite element library: design, features, and insights. *Comput. Math. Appl.* **81**, 407–422. (doi:10.1016/j.camwa.2020.02.022)
36. Maier M, Margetis D, Luskin M. 2017 Dipole excitation of surface plasmon on a conducting sheet: finite element approximation and validation. *J. Comp. Phys.* **339**, 126–145. (doi:10.1016/j.jcp.2017.03.014)
37. Hernandez V, Roman JE, Vidal V. 2005 SLEPc: a scalable and flexible toolkit for the solution of eigenvalue problems. *ACM Trans. Math. Softw.* **31**, 351–362. (doi:10.1145/1089014.1089019)
38. Rannacher R, Blum H. 1987/1988 Extrapolation techniques for reducing the pollution effect of reentrant corners in the finite element method. *Numerische Mathematik* **52**, 539–564. (doi:10.1007/BF01400891)
39. McLean W. 2000 *Strongly elliptic systems and boundary integral equations*. Cambridge, UK: Cambridge University Press.
40. Gilbarg D, Trudinger NS. 2015 *Elliptic partial differential equations of second order*. Berlin, Germany: Springer.
41. Yan Y, Sloan IH. 1988 On integral equations of the first kind with logarithmic kernels. *J. Integral Equ. Appl.* **1**, 549–579.
42. Stephan EP. 1987 Boundary integral equations for screen problems in $\mathbb{R}^3$. *Integral Equ. Operator Theory* **10**, 236–257. (doi:10.1007/BF01199079)
43. Wendland WL, Stephan E, Darmstadt, Hsiao GC. 1979 On the integral equation method for the plane mixed boundary value problem of the Laplacian. *Math. Methods Appl. Sci.* **1**, 265–321. (doi:10.1002/mma.1670010302)